

Gemini/GMOS photometry of intermediate-age star clusters in the Large Magellanic Cloud

Andrés E. Piatti,^{1,2*} Stefan C. Keller,³ A. Dougal Mackey³ and Gary S. Da Costa³

¹*Observatorio Astronómico, Universidad Nacional de Córdoba, Laprida 854, 5000 Córdoba, Argentina*

²*Consejo Nacional de Investigaciones Científicas y Técnicas, Av. Rivadavia 1917, C1033AAJ Buenos Aires, Argentina*

³*Research School of Astronomy and Astrophysics, Australian National University, Canberra 2611, Australia*

Accepted 2014 July 29. Received 2014 July 10; in original form 2014 May 9

ABSTRACT

We present Gemini South GMOS g , i photometry of 14 intermediate-age Large Magellanic Cloud (LMC) star clusters, namely: NGC 2155, 2161, 2162, 2173, 2203, 2209, 2213, 2231, 2249, Hodge 6, SL 244, 505, 674, and 769, as part of a continuing project to investigate the extended main-sequence turn-off (EMSTO) phenomenon. Extensive artificial star tests were made over the observed field of view. These tests reveal the observed behaviour of photometric errors with magnitude and crowding. The cluster stellar density radial profiles were traced from star counts over the extent of the observed field. We adopt cluster radii and build colour–magnitude diagrams (CMDs) with cluster features clearly identified. We used the cluster (g , $g - i$) CMDs to estimate ages from the matching of theoretical isochrones. The studied LMC clusters are confirmed to be intermediate-age clusters, which range in age $9.10 < \log(t) < 9.60$. NGC 2162 and NGC 2249 look like new EMSTO candidates, in addition to NGC 2209, on the basis of having dual red clumps.

Key words: techniques: photometric – galaxies: individual: LMC – Magellanic Clouds.

1 INTRODUCTION

The massive stellar clusters in the Large Magellanic Cloud (LMC) possess a wide range of ages (10^6 – 10^{10} yr) though as well as a well-established dearth of clusters with ages between ~ 3 – 4×10^9 and 10^{10} yr (see, e.g. Da Costa 1991; Baumgardt et al. 2013). This makes the LMC an important testing ground for theories of how massive star clusters form and evolve both dynamically and possibly chemically. Because of the proximity of the LMC, massive clusters of intermediate age (i.e. 1–3 Gyr) are readily accessible for detailed study. The cluster NGC 1846 ($M \approx 10^5 M_{\odot}$; age ≈ 1.8 Gyr; $[\text{Fe}/\text{H}] \approx -0.4$) was found by Mackey & Broby Nielsen (2007) to possess a colour–magnitude diagram (CMD) exhibiting two distinct main-sequence turn-offs (MSTOs). The width of the red giant branch (RGB) is small, which indicates there is no significant internal spread in $[\text{Fe}/\text{H}]$. The cluster is consistent with the presence of two stellar populations with ages 300 Myr apart (Mackey et al. 2008).

Searches of the *HST*/ACS archive (Mackey et al. 2008; Milone et al. 2009) revealed another 10 LMC clusters of ages between 1 and 2.5 Gyr that exhibit unusual MSTOs. The MSTO region of these clusters may be bifurcated or much more extended than can be accounted for by photometric errors. Binary stars seem to contribute

at different levels to the broadness around the MSTO (Goudfrooij et al. 2009; Milone et al. 2009; Yang et al. 2011). Similarly, stellar rotation appears in some works as an unlikely solution (Girardi, Rubele & Kerber 2009), or performs equally well like age spread (Li, de Grijs & Deng 2014), or is preferred (Bastian & de Mink 2009). Milone et al. report that 11 of 16 (i.e. 70 ± 25) per cent intermediate-age clusters possess this phenomenon.

Keller, Mackey & Da Costa (2011) have simulated stellar populations with a range of luminosities and star formation histories. These simulations show that a cluster with bimodal star formation history featuring a 200 Myr hiatus would be undetectable to existing ACS photometry of LMC clusters once the age of the cluster exceeds 2.3 Gyr. This is a consequence of the fact that in increasingly older clusters, the difference in age between the constituent stellar populations represents a diminishing fraction of the cluster age, hence the multiple populations become increasingly harder to resolve photometrically. The fact that the multiple-MSTO phenomenon is only detected in globular clusters (GCs) younger than 2.5 Gyr is therefore not unexpected. Indeed, it is plausible that the production of multiple populations is an evolutionary phase for the majority of massive clusters, although it is not seen in some massive younger clusters (Bastian & Silva-Villa 2013; Cabrizi-Ziri et al. 2014). The currently known multiple MSTO clusters possess another outstanding feature. The extended main-sequence turn-off (EMSTO) clusters show a tendency to have larger core radii than non-EMSTO clusters (Keller et al. 2011).

*E-mail: andres@oac.uncor.edu

Table 1. Observation log of selected clusters.

Star cluster	α_{2000} (h m s)	δ_{2000} ($^{\circ}$ ' ")	Filter	Exposures (times \times s)	Airmass	Seeing (arcsec)
NGC 2155	05 58 33	-65 28 37	<i>g</i>	4 \times 150 + 4 \times 30	1.24–1.25	0.42–0.52
			<i>i</i>	4 \times 150 + 4 \times 15	1.25–1.27	0.35–0.41
NGC 2161	05 55 42	-74 21 14	<i>g</i>	4 \times 150 + 4 \times 30	1.38	0.46–0.65
			<i>i</i>	4 \times 150 + 4 \times 15	1.38	0.38–0.43
NGC 2162	06 00 31	-63 43 17	<i>g</i>	4 \times 150 + 4 \times 30	1.53–1.59	0.55–0.64
			<i>i</i>	4 \times 150 + 4 \times 15	1.60–1.66	0.52–0.72
NGC 2173	05 57 58	-72 58 43	<i>g</i>	4 \times 150 + 4 \times 30	1.36	0.44–0.49
			<i>i</i>	4 \times 150 + 4 \times 15	1.36–1.37	0.35–0.42
NGC 2203	06 04 42	-75 26 16	<i>g</i>	4 \times 150 + 4 \times 30	1.46–1.48	0.55–0.59
			<i>i</i>	4 \times 150 + 4 \times 15	1.48–1.50	0.48–0.59
NGC 2209	06 08 34	-73 50 28	<i>g</i>	10 \times 145 + 4 \times 30	1.47–1.57	0.59–0.75
			<i>i</i>	6 \times 137 + 4 \times 15	1.52–1.58	0.43–0.58
NGC 2213	06 10 42	-71 31 44	<i>g</i>	4 \times 150 + 4 \times 30	1.43–1.46	0.55–0.58
			<i>i</i>	4 \times 150 + 4 \times 15	1.46–1.49	0.43–0.45
NGC 2231	06 20 44	-67 31 05	<i>g</i>	5 \times 150 + 8 \times 30	1.43–1.46	0.58–0.68
			<i>i</i>	4 \times 150 + 5 \times 15	1.47–1.51	0.58–0.64
NGC 2249	06 25 49	-68 55 12	<i>g</i>	12 \times 300 + 15 \times 40	1.27–1.43	0.52–0.68
			<i>i</i>	5 \times 280 + 5 \times 40	1.28–1.29	0.42–0.48
Hodge 6	05 42 17	-71 35 28	<i>g</i>	9 \times 300 + 8 \times 40	1.33–1.40	0.43–0.78
			<i>i</i>	6 \times 280 + 6 \times 40	1.33–1.40	0.48–0.58
SL 244	05 07 37	-68 32 30	<i>g</i>	4 \times 60	1.48–1.50	0.69–0.77
			<i>i</i>	4 \times 30	1.40–1.41	0.48–0.55
SL 505	05 28 50	-71 38 00	<i>g</i>	4 \times 60	1.45–1.46	0.63–0.71
			<i>i</i>	4 \times 30	1.39–1.40	0.48–0.58
SL 674	05 43 20	-66 15 42	<i>g</i>	4 \times 60	1.40–1.42	0.57–0.70
			<i>i</i>	4 \times 30	1.32–1.33	0.47–0.53
SL 769	05 53 23	-70 04 18	<i>g</i>	4 \times 60	1.40–1.41	0.63–0.64
			<i>i</i>	4 \times 30	1.35	0.45–0.55

In order to investigate the frequency of occurrence of the multiple-MSTO phenomenon in the LMC cluster population, we have built an age- and luminosity-limited sample with which to examine if the formation of multiple populations is a general phase of cluster evolution, one possibly related to the puzzling multiple populations seen in ancient Galactic GCs (see for example, Carretta et al. 2010). In this paper, we present a photometric data set for a number of clusters in the sample for which high-quality CMDs were previously unavailable. Although we defer a detailed analysis on the presence or absence of the extended MSTO phenomenon in these clusters to a forthcoming paper (Keller et al., in preparation), we investigate the status of each cluster on the basis of matching single stellar population (SSP) isochrones to their respective CMDs. We thus provide estimates of the mean cluster ages, which will assist in the analysis of the role of cluster core radii, the degree of MSTO broadness, dynamical status of the clusters, etc. Results from this programme for the LMC cluster NGC 2209 have been published in Keller, Mackey & Da Costa (2012). In Section 3, we present the derived cluster photometry, followed by derivation of the fundamental cluster parameters of age and metallicity, and spatial extent in Section 4.

2 OBSERVATIONS AND DATA REDUCTION

We obtained images of 14 candidate LMC intermediate-age clusters with the Gemini South telescope and the GMOS-S instrument through *g* and *i* filters. In imaging mode, GMOS-S has a field of view of approximately 5.5 arcmin \times 5.5 arcmin at a scale of 0.146 arcsec per (2×2 binned) pixel. The detector is a 3×1 mosaic of $2 \text{ K} \times 4 \text{ K}$ EEV CCDs. Observations were executed in queue mode (under

programmes GS-2011A-Q-43, GS-2012A-Q-15, and GS-2013A-Q-17) which enabled the data to be obtained in excellent seeing (0.35–0.78 arcsec FWHM) and under photometric conditions. The log of observations is presented in Table 1, where the main astrometric, photometric, and observational information is summarized. Several images were taken in each filter (*g*, *i*), as we judged that the dynamic range and accuracy required to suit our science goals could be met most efficiently this way. Most of the selected fields have shorter and longer exposure times to provide coverage of bright cluster RGB stars as well as stars at least two magnitudes below the MSTO in order to search for the presence of the extended MSTO phenomenon.

The data reduction followed the procedures documented in the Gemini Observatory webpage¹ and utilized the GEMINI/GMOS package in IRAF.² We performed overscan, trimming, bias subtraction, flattened all data images, etc., once the calibration frames (zeros and flats) were properly combined.

Observations of photometric standard stars were included in the baseline calibrations for GMOS. The standard stars were chosen from the standard star catalogue calibrated directly in the SDSS system.³ For programme GS-2011A-Q-43, the standard fields 160100–600000, E5_b, E3_a, PG1633+099, and LSE 259 were observed during the same nights as for NGC 2155, 2161, 2162, 2173, 2203, 2209, 2213, and 2231. NGC 2231 was

¹ <http://www.gemini.edu>

² IRAF is distributed by the National Optical Astronomy Observatories, which is operated by the Association of Universities for Research in Astronomy, Inc., under contract with the National Science Foundation.

³ <http://www-star.fnal.gov>

Table 2. CCD gi data of stars in the field of NGC 2155. The complete table is available online as Supporting Information.

Star	RA (J2000) (h:m:s)	Dec. (J2000) ($^{\circ}$ ' ")	g (mag)	$\sigma(g)$ (mag)	$g - i$ (mag)	$\sigma(g - i)$ (mag)	n
9	05:58:13.149	-65:31:27.72	22.835	0.014	0.275	0.022	4
10	05:58:09.841	-65:30:31.02	24.139	0.023	0.347	0.067	4
11	05:58:03.581	-65:28:43.59	24.139	0.038	0.465	0.053	3
–	–	–	–	–	–	–	–

observed during two different nights, so that we used its photometry for additional controls. The calibrated photometry for NGC 2173 and 2209 have been previously published in Keller et al. (2012). For programme GS-2013A-Q-17, the standard fields 060000–300000 and 160100–600000 were observed during the same night as for clusters SL 244, 505, 674, and 769. Images of standard star fields were not observed as a regular-based instrument monitoring (programme objects NGC 2249 and Hodge 6). However, we have paid particular care when using the calibrations derived (see also, <http://www.gemini.edu/node/10625?q=node/10445>) assuming that the atmospheric extinction was close to the median value for Cerro Pachon.

Independent magnitude measures of standard stars were derived per filter using the APPHOT task within IRAF, in order to secure

the transformation from the instrumental to the SDSS gi standard system. Standard stars were distributed over an area similar to that of the GMOS array, so that we measured magnitudes of standard stars in each of the three chips. The relationships between instrumental and standard magnitudes were obtained by fitting the following equations:

$$g = g_1 + g_{\text{std}} + g_2 \times X_g + g_3 \times (g - i)_{\text{std}}, \quad (1)$$

$$i = i_1 + i_{\text{std}} + i_2 \times X_i + i_3 \times (g - i)_{\text{std}}, \quad (2)$$

where g_j , and i_j ($j = 1, 3$) are the fitted coefficients, and X represents the effective airmass. We solved the transformation equations with the FITPARAMS task in IRAF. The root-mean square (rms) errors from the transformation to the standard system were 0.011 mag

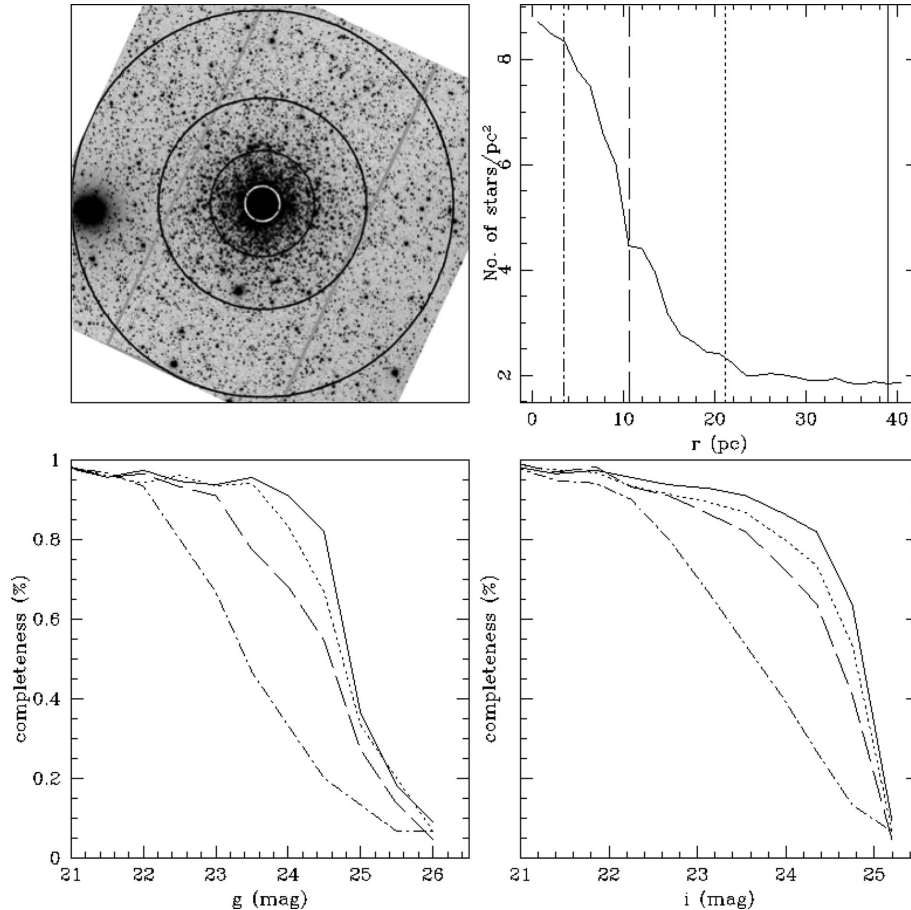


Figure 1. i image with the LMC cluster NGC 2173 and four circles of 100, 300, 600, and 1100 pixels overlotted (upper left). North is up and east is to the left. The cluster density profile (upper right) and the completeness level in g (bottom left) and i (bottom right) bands are also shown for different circular rings: 0–100 pixels (dot-dashed line); 100–300 pixels (dashed line); 300–600 pixels (dotted line), and 600–1100 pixels (solid line).

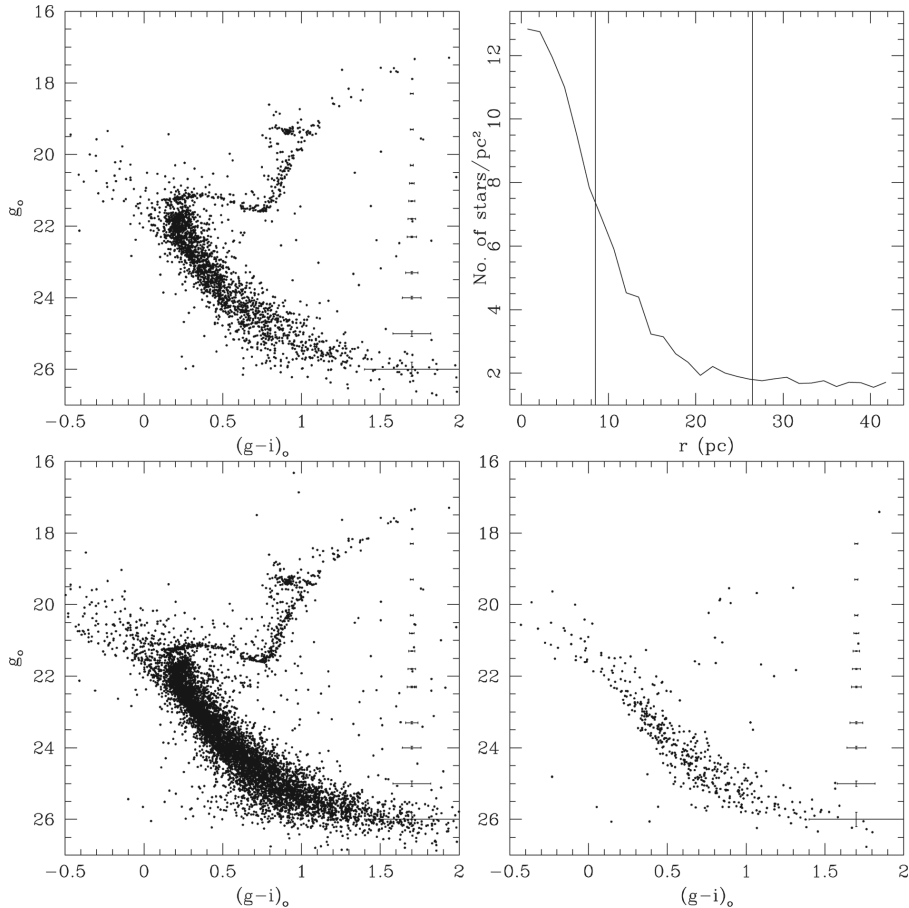


Figure 2. CMDs for stars in NGC 2155 distributed within circles centred on the cluster and radii r_{HM} (upper left) and r_{cls} (bottom left), and that for surrounding field stars distributed within a ring of area πr_{HM}^2 (bottom right). The cluster density profile with the radii at r_{HM} and r_{cls} indicated is also shown (upper right).

for g and 0.013 for i , respectively, indicating excellent photometric quality.

The stellar photometry was performed using the star-finding and point spread function (PSF) fitting routines in the DAOPHOT/ALLSTAR suite of programs (Stetson, Davis & Crabtree 1990). For each frame, a quadratically varying PSF was derived by fitting ~ 60 stars, once the neighbours were eliminated using a preliminary PSF derived from the brightest, least contaminated 20–30 stars. Both groups of PSF stars were interactively selected. We then used the ALLSTAR program to apply the resulting PSF to the identified stellar objects and to create a subtracted image which was used to find and measure magnitudes of additional fainter stars. This procedure was repeated three times for each frame. Finally, we computed aperture corrections from the comparison of PSF and aperture magnitudes by using the neighbour-subtracted PSF star sample. After deriving the photometry for all detected objects in each filter, a cut was made on the basis of the parameters returned by DAOPHOT. Only objects with $\chi < 2$, photometric error less than 2σ above the mean error at a given magnitude, and $|\text{SHARP}| < 0.5$ were kept in each filter (typically discarding about 10 per cent of the objects), and then the remaining objects in the g and i lists were matched with a tolerance of 1 pixel and raw photometry obtained.

We combined all the independent instrumental magnitudes using the stand-alone DAOMATCH and DAOMASTER programs.⁴ As a result, we

produced one data set per cluster containing the x - and y -coordinates for each star, and different $(g, g - i)$ pairs according to the number of frames obtained per filter. We did not combine (g, i) shorter with longer exposures, but treat them separately. The gathered photometric information were standardized using equations (1) and (2). We finally averaged standard magnitudes and colours of stars measured several times. The resulting standardized photometric tables consist of a running number per star, equatorial coordinates, the averaged g magnitudes and $g - i$ colours, their respective rms errors $\sigma(g)$ and $\sigma(g - i)$, and the number of observations per star. We adopted the photometric errors provided by ALLSTAR for stars with only one measure. Tables 2–15 provide this information for NGC 2155, 2161, 2162, 2173, 2203, 2209, 2213, 2231, 2249, Hodge 6, SL 244, 505, 674, and 769, respectively. Only a portion of Table 2 is shown here for guidance regarding their form and content. The whole content of Tables 2–15 is available in the online version of the journal on Oxford journals website at <http://access.oxfordjournals.org>.

We first examined the quality of our photometry in order to evaluate the influence of the photometric errors, crowding effects and the detection limit on the cluster fiducial characteristics in the CMDs. To do this, we performed artificial star tests on a long exposure image per filter and per cluster to derive the completeness level at different magnitudes. We used the stand-alone ADDSTAR program in the DAOPHOT package (Stetson et al. 1990) to add synthetic stars, generated bearing in mind the colour and magnitude distributions of the stars in the CMDs (mainly along the main sequence (MS) and the RGB), as well as the radial stellar density profiles

⁴ Program kindly provided by P.B. Stetson.

of the cluster fields. We added a number of stars equivalent to ~ 5 per cent of the measured stars in order to avoid significantly more crowding synthetic images than in the original images. On the other hand, to avoid small number statistics in the artificial-star analysis, we created five different images for each one used in the artificial star tests. Utilizing the tabulated gains for the GMOS devices, we were able to simulate the Poisson noise in each stellar image.

We then repeated the same steps to obtain the photometry of the synthetic images as described above, i.e. performing three passes with the DAOPHOT/ALLSTAR routines, making a cut on the basis of the parameters returned by DAOPHOT, etc. The errors and star-finding efficiency was estimated by comparing the output and the input data for these stars – within the respective magnitude and colour bins – using the DAOMATCH and DAOMASTER tasks. In Fig. 1, we show the resultant completeness fractions as a function of magnitude for NGC 2173, which is a representative cluster in our sample when considering simultaneously the largest extent, crowding and number of measured stars. Fig. 1 shows that the 50 per cent completeness level is reached at $g, i \sim 23.5\text{--}25.0$, depending on the distance from the cluster centre. On the other hand, by using the theoretical isochrones of Mackey et al. (2008) and the LMC distance modulus $(m - M)_o = 18.49$ (de Grijs, Wicker & Bono 2014), we concluded that the MSTO of star clusters with ages between 1 and 3 Gyr is located at $g \sim 20\text{--}21$ mag. Thus, we conclude that our photometry is able to reach the 50 per cent completeness level 2–3 mag below the MSTO for the innermost cluster regions

(distance to the cluster centre $\leq r_{\text{HM}}/4$ where r_{HM} is a measure of the cluster size defined in the next section). The behaviour of $\sigma(g)$ and $\sigma(g - i)$ is represented by error bars in the CMDs shown in Figs 2–15.

3 ANALYSIS OF THE CMDs

In Figs 2–15, we show the CMDs of stars in the field of NGC 2155, 2161, 2162, 2173, 2203, 2209, 2213, 2231, 2249, Hodge 6, SL 244, 505, 674, and 769, respectively. The most obvious traits in each cluster CMD are the long cluster MS which extends over a range of approximately 4–5 mag in g , the cluster red clump (RC) and RGB. In some cases, a populous cluster subgiant branch (SGB) is also visible (e.g. NGC 2155; Fig. 2). The RC is not tilted in any of the studied clusters – except SL 244 – so that differential reddening can be assumed to be negligible along the lines of sight. However, NGC 2162, 2209, and 2249 have clear dual RCs, a feature seen in star clusters exhibiting the EMSTO phenomenon (Milone et al. 2009). Keller et al. (2012) discuss the parameters of the EMSTO evident in NGC 2209. The consequences of the detection of the EMSTO phenomenon or otherwise in this set of clusters is the focus of a separate paper (Keller et al. in preparation), for which we will use as inputs the mean cluster age estimates derived in this work.

We determined the cluster geometrical centres in order to obtain circular extracted CMDs where the fiducial features of the clusters

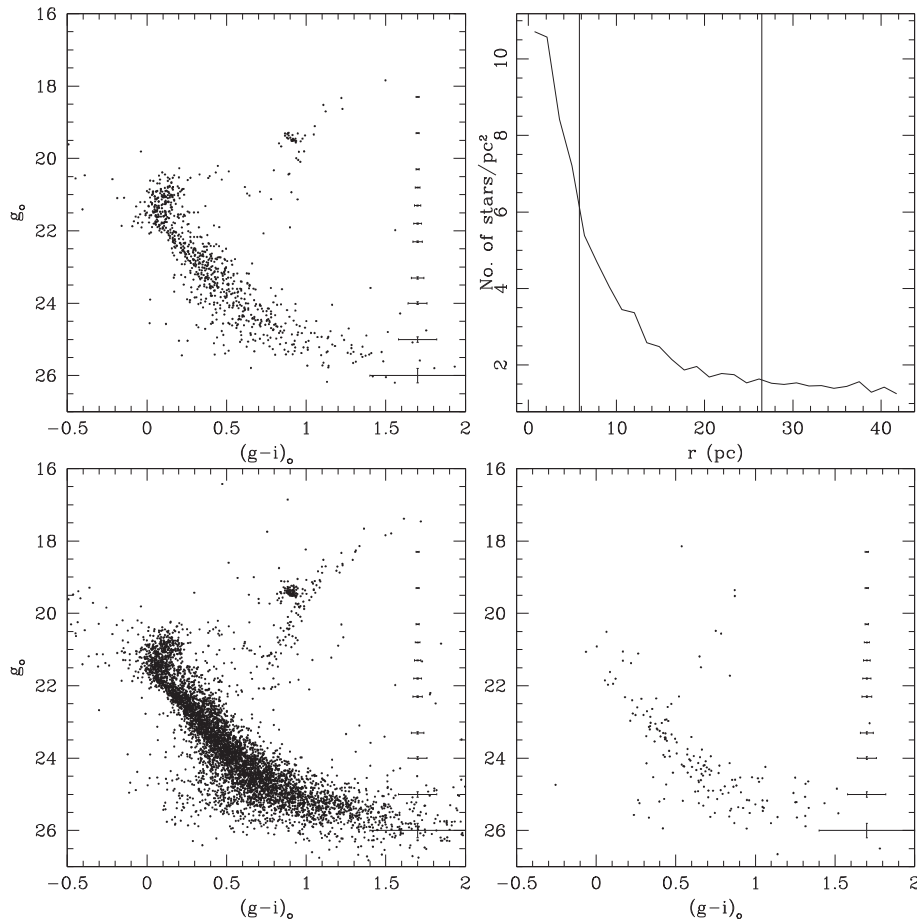


Figure 3. Idem as Fig. 2 for NGC 2161.

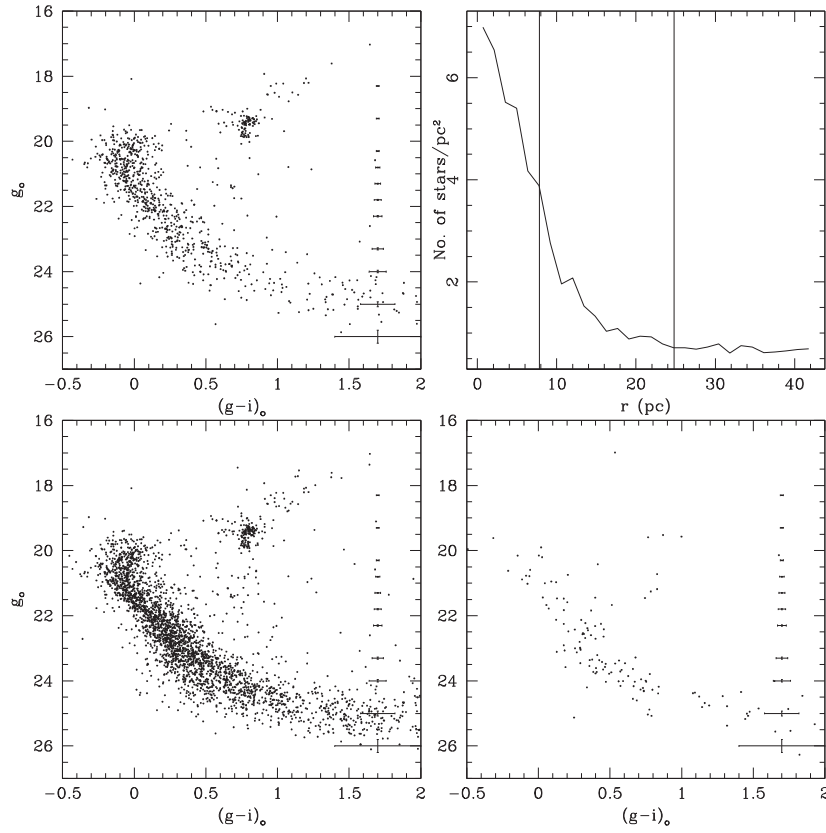


Figure 4. Idem as Fig. 2 for NGC 2162.

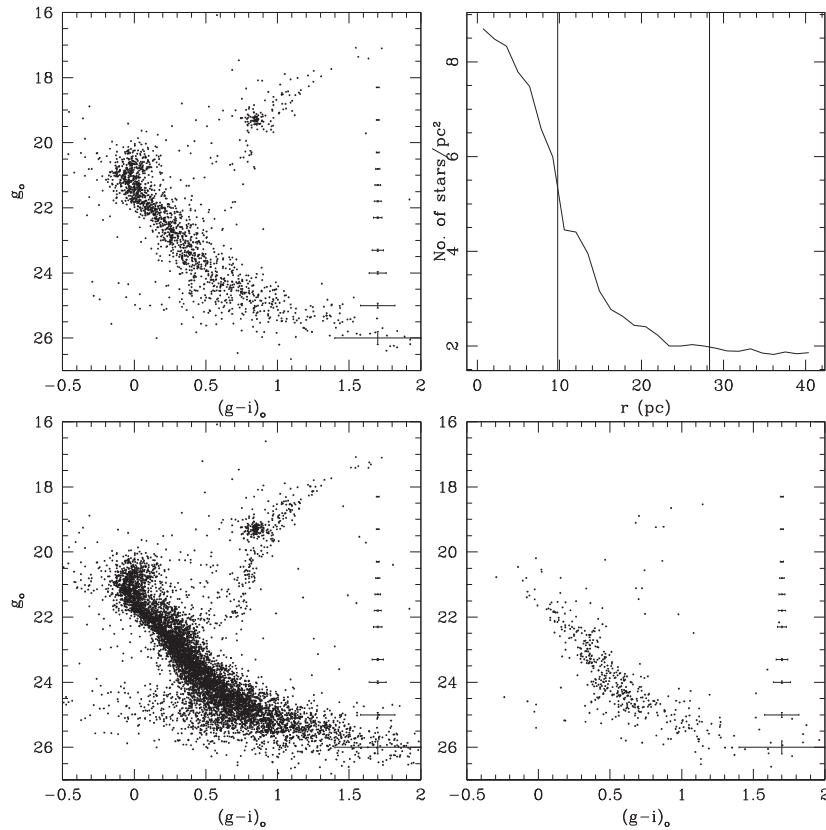


Figure 5. Idem as Fig. 2 for NGC 2173.

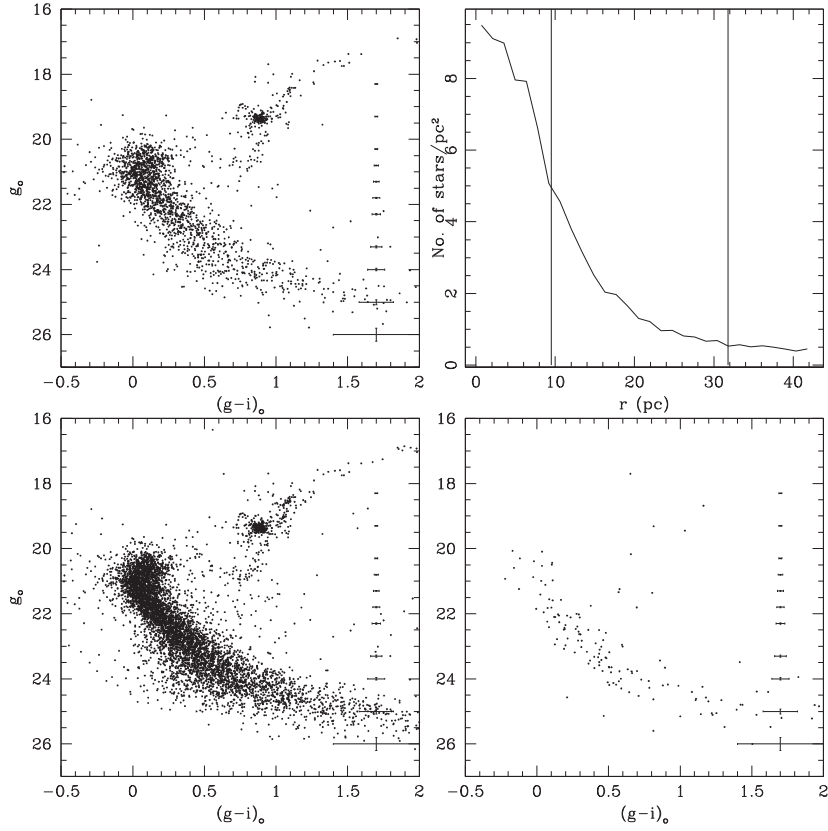


Figure 6. Idem as Fig. 2 for NGC 2203.

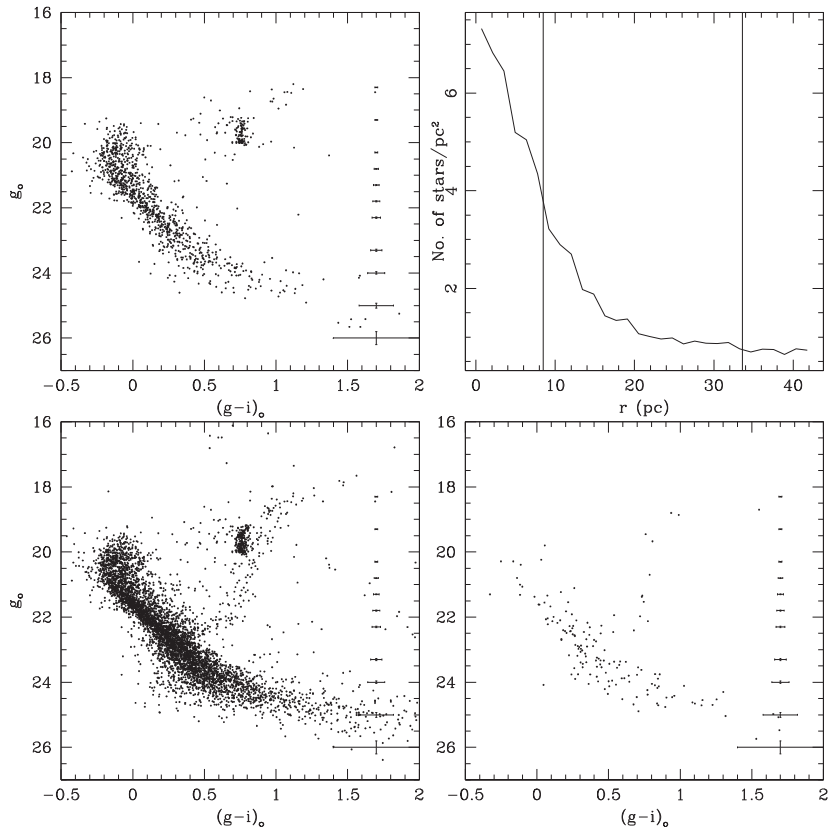


Figure 7. Idem as Fig. 2 for NGC 2209.

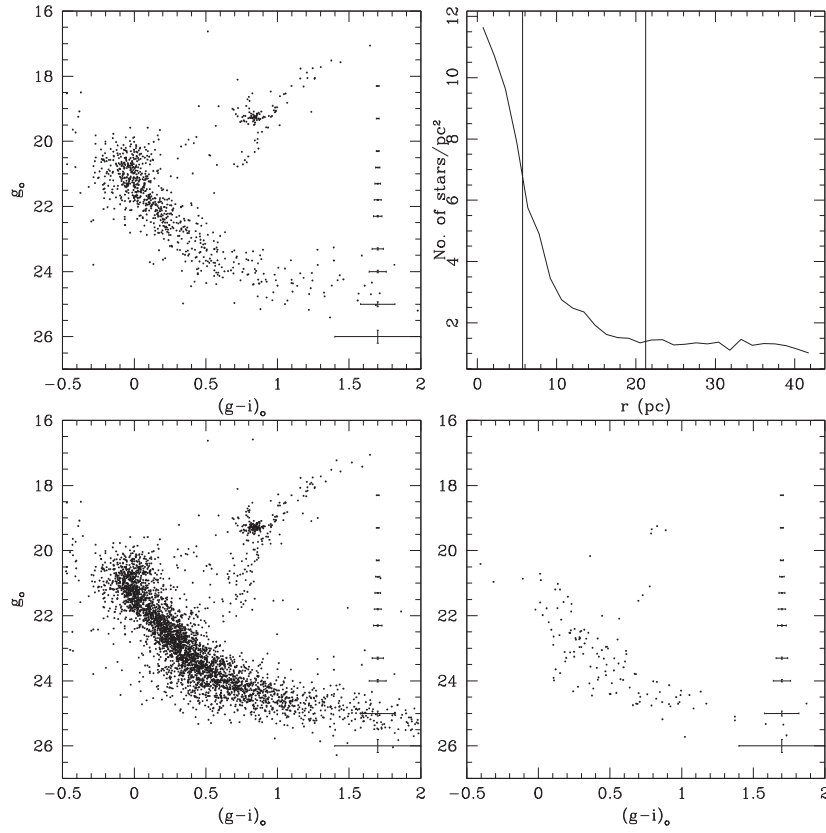


Figure 8. Idem as Fig. 2 for NGC 2213.

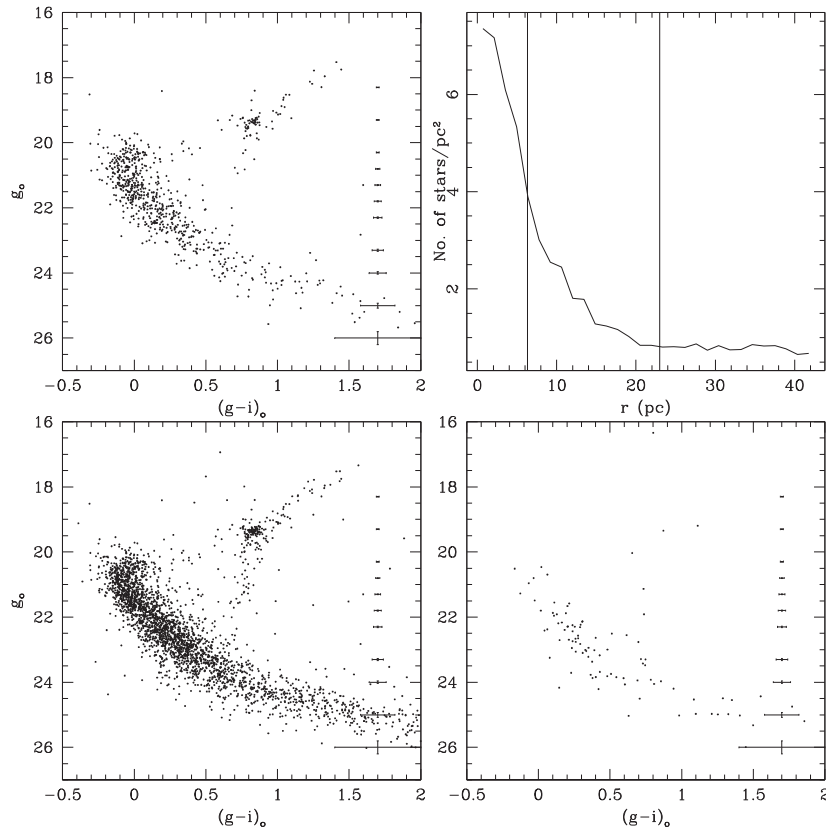


Figure 9. Idem as Fig. 2 for NGC 2213.

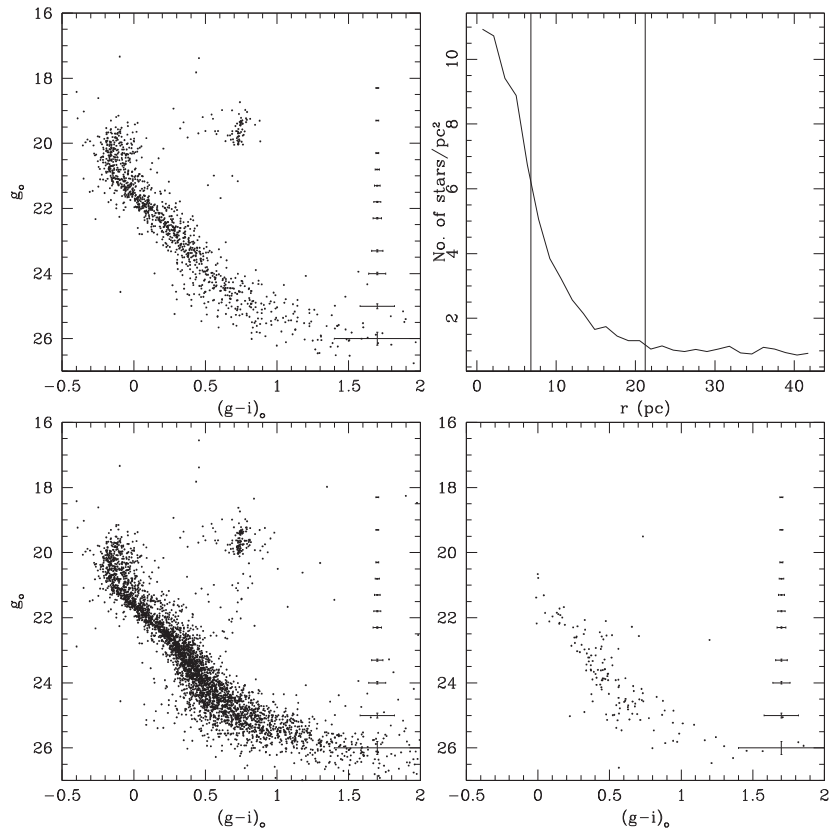


Figure 10. Idem as Fig. 2 for NGC 2249.

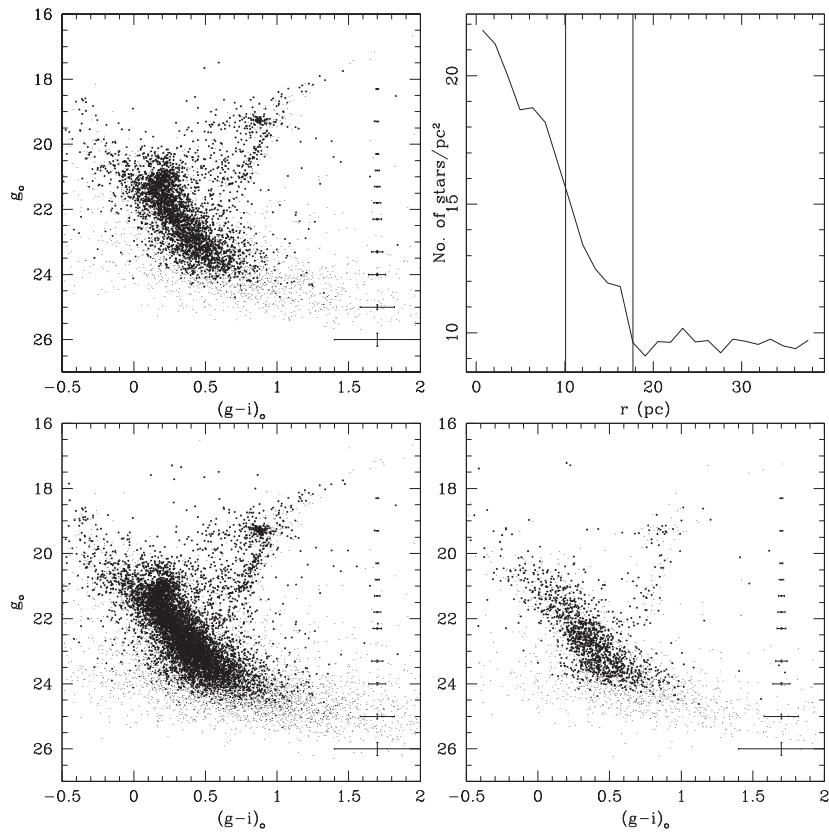


Figure 11. Idem as Fig. 2 for Hodge 6. Small points correspond to stars with a number of observations less than 5.

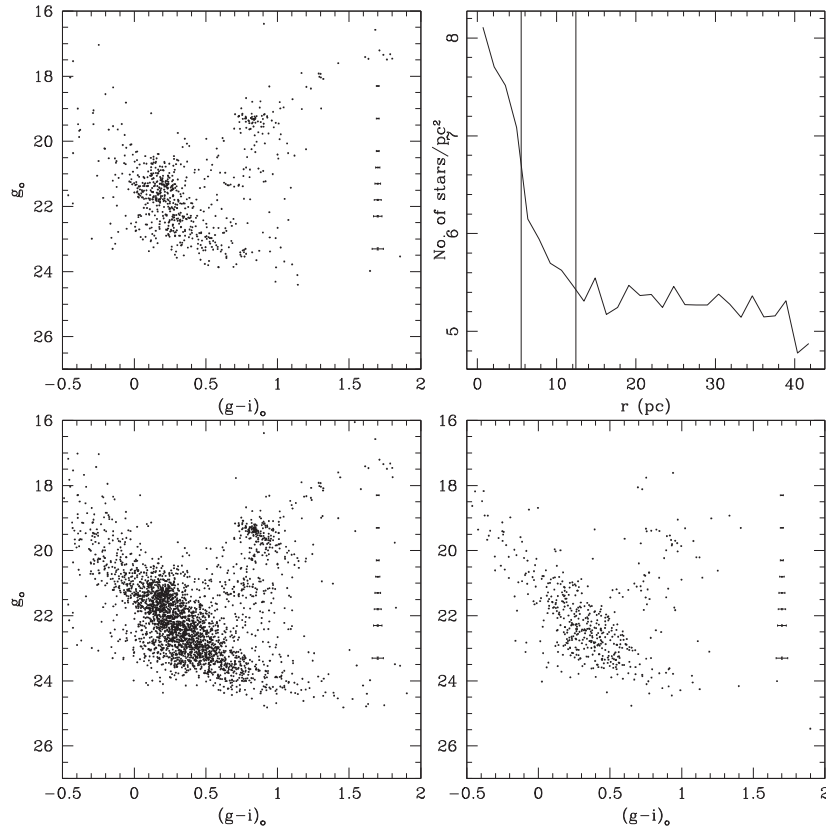


Figure 12. Idem as Fig. 2 for SL 244.

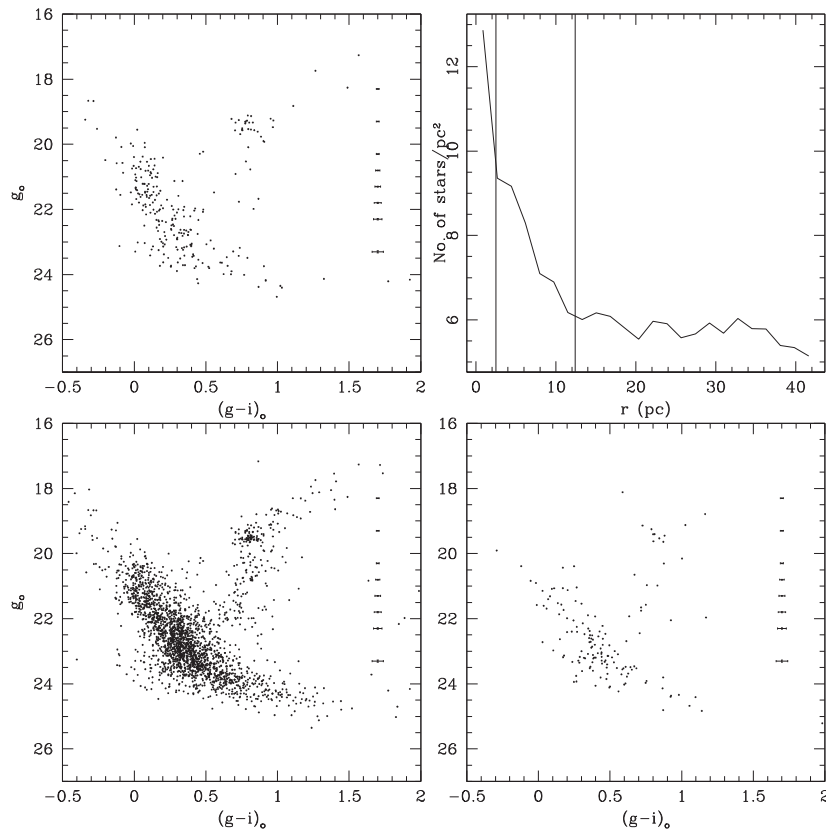


Figure 13. Idem as Fig. 2 for SL 505.

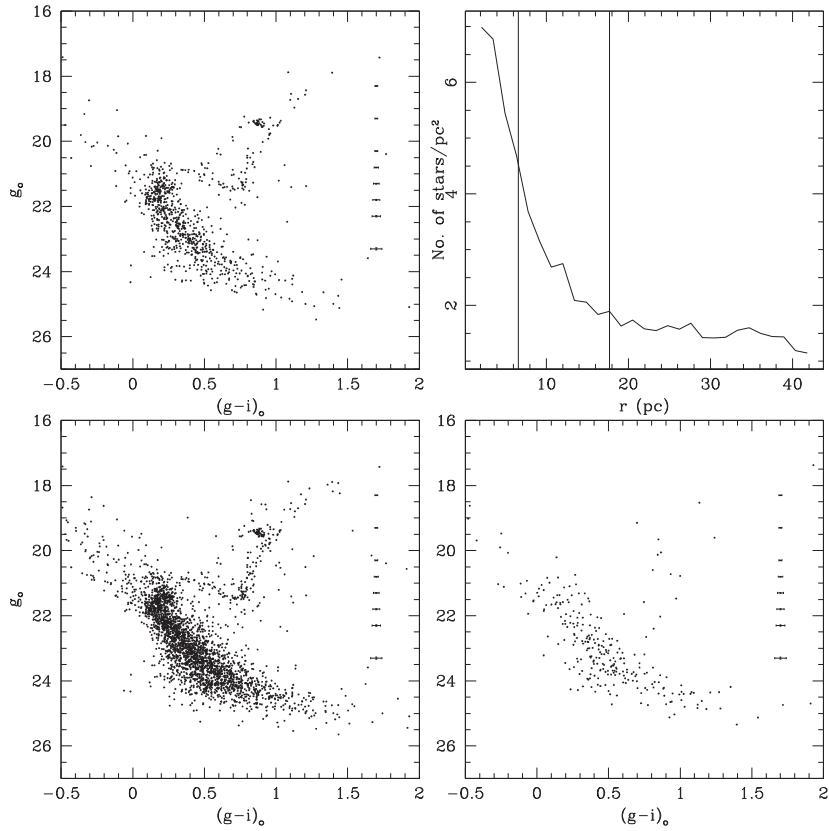


Figure 14. Idem as Fig. 2 for SL 674.

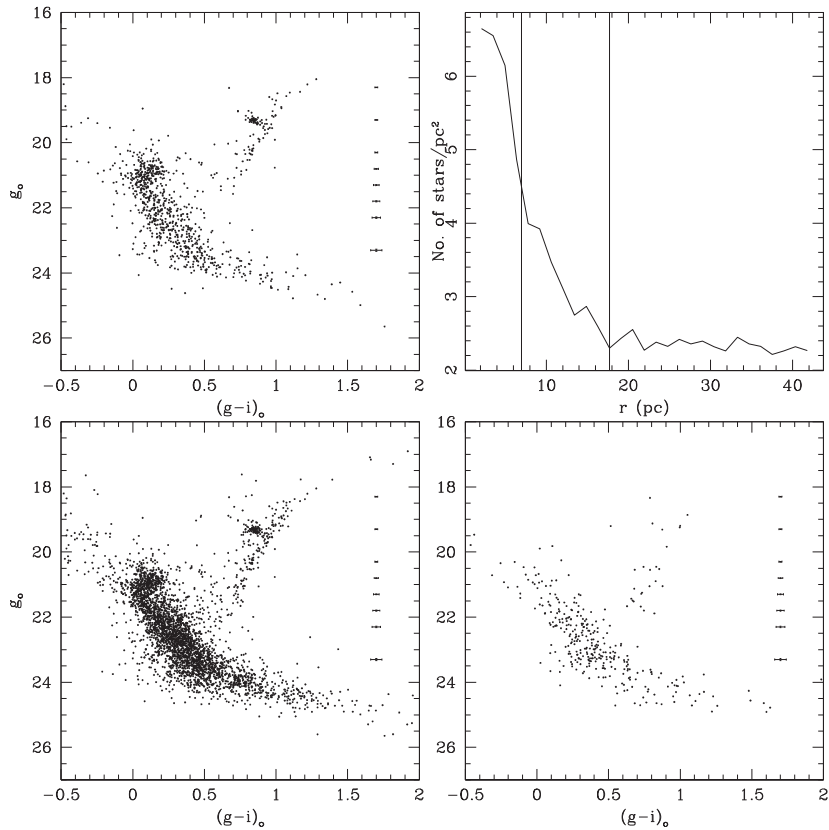


Figure 15. Idem as Fig. 2 for SL 679.

Table 16. Fundamental properties of LMC star clusters.

Star cluster	r_{HM} (pc)	r_{cls} (pc)	ρ	$E(B - V)$ (mag)	$\log(t)$	$\log(t)$ (literature)	Ref.
NGC 2155	8.5	26.5	3.1	0.03	9.50 ± 0.05	9.56 ± 0.08	2
NGC 2161	5.8	26.5	2.8	0.12	9.35 ± 0.05	9.04 ± 0.12	3
NGC 2162	7.8	24.8	4.5	0.03	9.20 ± 0.05	9.11 ± 0.14	1
NGC 2173	9.8	28.3	1.7	0.09	9.25 ± 0.05	9.33 ± 0.08	1
NGC 2203	9.5	31.8	8.1	0.11	9.30 ± 0.05	–	
NGC 2209	8.5	33.6	4.2	0.11	9.15 ± 0.05	9.18 ± 0.09	4
NGC 2213	5.7	21.2	3.7	0.11	9.25 ± 0.05	9.20 ± 0.11	1
NGC 2231	6.3	23.0	4.0	0.06	9.20 ± 0.05	9.18 ± 0.11	1
NGC 2249	6.8	21.2	4.1	0.07	9.15 ± 0.05	8.82 ± 0.30	1
Hodge 6	10.1	17.7	0.6	0.09	9.40 ± 0.10	–	
SL 244	5.5	12.4	0.3	0.07	9.40 ± 0.10	9.18 ± 0.09	5
SL 505	2.5	12.4	0.6	0.08	9.30 ± 0.10	9.18 ± 0.09	5
SL 674	6.6	17.7	1.3	0.05	9.45 ± 0.05	9.36 ± 0.06	5
SL 769	7.0	17.7	0.9	0.08	9.35 ± 0.10	9.25 ± 0.07	6

Ref.: (1) Baumgardt et al. (2013), (2) Piatti et al. (2002), (3) Piatti et al. (2011a), (4) Piatti et al. (1999), (5) Geisler et al. (2003), (6) Bica et al. (1998).

could be clearly seen. The coordinates of the cluster centres and their estimated uncertainties were determined by fitting Gaussian distributions to the star counts in the x - and y -directions for each cluster. The fits of the Gaussians were performed using the `NGAUSS-FIT` routine in the `STSDAS/IRAF` package. We adopted a single Gaussian and fixed the constant to the corresponding background levels (i.e. stellar field densities assumed to be uniform) and the linear terms to zero. The centre of the Gaussian, its amplitude and its full width at half-maximum (FWHM) acted as variables. The number of stars projected along the x - and y -directions were counted within intervals of 40 pixel wide. In addition, we checked that using spatial bins from 20 to 60 pixels does not result in significant changes in the derived centres. Cluster centres were finally determined with a typical standard deviation of ± 10 pixels (~ 0.3 pc) in all cases.

We then constructed the cluster radial profiles based on star counts previously performed within boxes of 40 pixels a side distributed throughout the whole field of each cluster. The selected size of the box allowed us to sample statistically the stellar spatial distribution. Thus, the number of stars per unit area at a given radius, r , can be directly calculated through the expression:

$$(n_{r+20} - n_{r-20}) / (m_{r+20} - m_{r-20}), \quad (3)$$

where n_j and m_j represent the number of stars and boxes included in a circle of radius j , respectively. Note that this method does not necessarily require a complete circle of radius r within the observed field to estimate the mean stellar density at that distance. This is an important consideration since having a stellar density profile which extends far away from the cluster centre allows us to estimate the background level with high precision. This is necessary to derive the cluster radius (r_{cls}), defined as the distance from the cluster centre where the combined cluster plus background stellar density profile is no longer readily distinguished from a constant background value within 1σ of its fluctuation, which typically led to uncertainties of $\sigma(r_{\text{cls}}) \approx 2$ pc. It is also helpful to measure the FWHM of the stellar density profile, which plays a significant role – from a stellar content point of view – in the construction of the cluster CMDs.

The resulting density profiles expressed as number of stars per unit area are shown in the upper right-hand panel of Figs 2–15. In these figures, we show the region around the centre of each

cluster out to ~ 2.7 arcmin (≈ 1100 pixels). The background region surrounding each cluster was delimited between the observed field boundaries and the cluster radius from the cluster’s centre. The vertical lines represent the radii at the FWHM (r_{HM}) and r_{cls} . The r_{cls} values were estimated by eye on the cluster radial profile plots according to the above definition, whereas r_{HM} were calculated from the half-maximum of the cluster radial profiles ($\sigma(r_{\text{HM}}) \approx 0.5$ pc). Note that these radial scales are not precisely defined, but that small changes in their values does not materially affect the appearance of the CMDs. We then constructed three CMDs covering different circular extractions around each cluster as shown in Figs 2–15 (upper-left, bottom-left, and bottom-right panels). The panels in the figures are arranged, from top to bottom and from left to right, in such a way that exhibit the stellar population variations from the innermost to the outermost regions of the cluster fields. We start with the CMD for stars distributed within $r < r_{\text{HM}}$, followed by that of the cluster regions delimited by $r < r_{\text{cls}}$ and finally by the adopted field CMD. The latter was built using a ring centred on the cluster of area πr_{HM}^2 and internal radius r_{cls} . We used the CMDs corresponding to the stars within r_{HM} as the cluster fiducial sequence references, and used those for r_{cls} to match theoretical isochrones. Some field star contamination is unavoidable, though. However, when comparing field and cluster CMDs, the differences in stellar content become noticeable, as can be seen from the upper-left and bottom-right panels of Figs 2–15. Particularly, the field CMDs contain much fewer stars and are dominated by relatively older MS star populations, although composed of stars within a wide age range. The CMDs of the cluster sample, on the other hand, exhibit distinct RCs characteristic of intermediate-age star clusters around 1–3 Gyr old.

4 DETERMINATION OF FUNDAMENTAL CLUSTER PARAMETERS

We computed $E(B - V)$ colour excesses by interpolating the extinction maps of Burstein & Heiles (1982, hereafter **BH**) using a grid of (l, b) values, with steps of $\Delta(l, b) = (0^\circ:01, 0^\circ:01)$ covering the observed fields. **BH** maps were obtained from H1 (21 cm) emission data for the southern sky. They furnish us with $E(B - V)$ colour excesses which depend on the Galactic coordinates. We obtained between 80 and 100 colour excesses per cluster field. Then, we

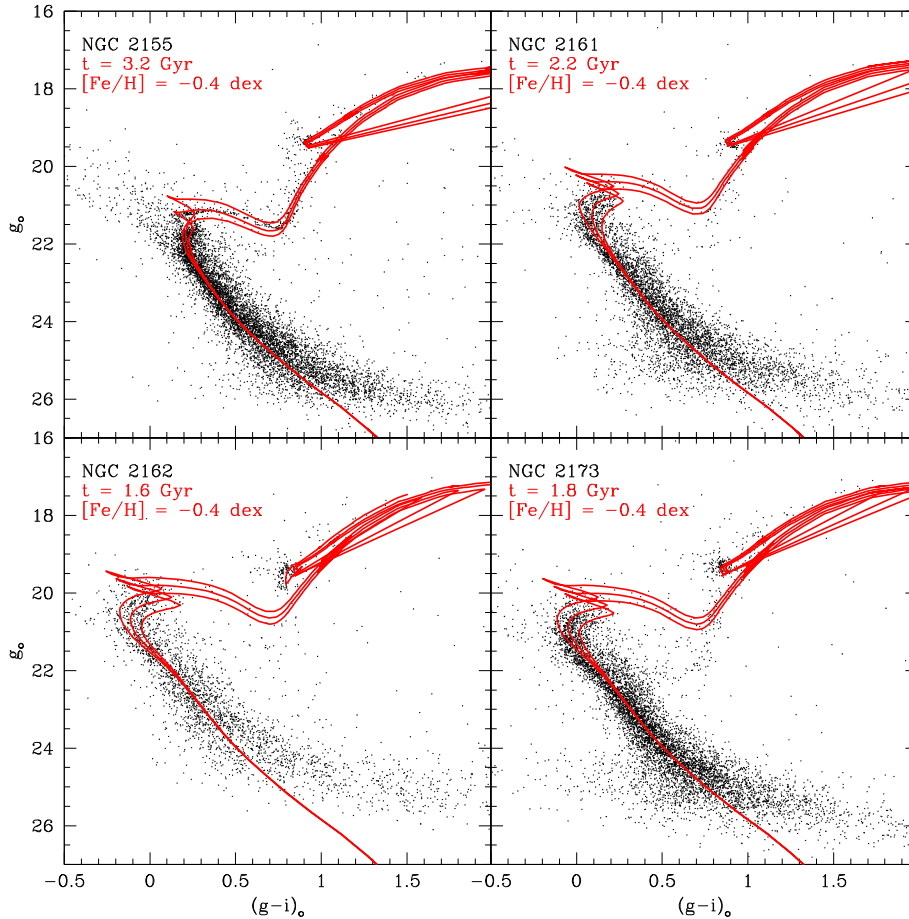


Figure 16. Theoretical isochrones from Bressan et al. (2012) superimposed on to LMC cluster CMDs. The youngest isochrone corresponds to $\log(t) - \sigma(\log(t))$ and metallicity (Z) listed in Table 16, whereas the isochrone separation is $\Delta(\log(t)) = 0.05$.

built histograms and calculated their centres and FWHMs. Since the FWHMs values turned out to be considerably low (~ 0.03 mag), we concluded that the interstellar absorption is uniform across the cluster fields. Our adopted reddenings are essentially identical to the BH reddenings tabulated for each cluster in NED.⁵ Five of our clusters in the periphery of the LMC also have reddenings tabulated in NED on the system of Schlafly & Finkbeiner (2011), which is a recalibration of the Schlegel, Finkbeiner & Davis (1998) reddenings. For these clusters the mean difference between our adopted reddenings and those from Schlafly & Finkbeiner (2011) is 0.01 mag with a standard deviation of 0.02 mag. Table 16 lists the adopted $E(B - V)$ colour excesses, from which we computed the $E(g - i)$ and A_g values using the $E(g - i)/E(B - V) = 1.621$ and $A_g/E(B - V) = 3.738$ ratios given by Cardelli, Clayton & Mathis (1989).

As for the cluster distance moduli, Subramanian & Subramanian (2009) find that the average depth for the LMC disc is 3.44 ± 1.16 kpc, so that the difference in apparent distance modulus – clusters could be placed in front of, or behind the LMC – could be as large as $\Delta((m - M)_o) \sim 0.15$ mag, if a value of 50 kpc is adopted for the mean LMC distance (de Grijs et al. 2014). Since a difference of 0.05 in $\log(t)$ (the difference between two close isochrones in the Bressan et al. 2012 models used here) implies a difference of ~ 0.25 mag in g , we decided to adopt the value of the LMC distance modulus $(m - M)_o = 18.49 \pm 0.09$ reported by

de Grijs et al. (2014) for all the clusters. Our simple assumption of adopting a unique value for the distance modulus for all the clusters should not dominate the error budget in our final results. In fact, when overplotting the zero-age main sequence (ZAMS) on the cluster CMDs, previously shifted by the corresponding $E(g - i)$ and $(m - M)_o = 18.49$, excellent matches were generally found.

In order to estimate the cluster ages, it must be taken into account that cluster metallicity plays an important role when matching theoretical isochrones. The distinction is mainly evident for the evolved RC and RGB phases. ZAMSs are often less affected by metallicity effects and can even exhibit imperceptible variations for a specific metallicity range within the expected photometric errors. We took advantage of the available theoretical isochrones computed for the SDSS photometric system to estimate cluster ages. We used the isochrones calculated with core overshooting included by the Padova group (Bressan et al. 2012). When we chose subsets of isochrones for different Z metallicity values to evaluate the metallicity effect in the cluster fundamental parameters, we adopted the most frequently used value of $[\text{Fe}/\text{H}] = -0.4$ dex ($Z = 0.006$, $Z_\odot = 0.0152$) for the intermediate-age LMC clusters studied to date Piatti & Geisler (2013, see their fig. 6).

We then selected a set of isochrones and superimposed them on the cluster CMDs, once they were properly shifted by the corresponding LMC distance modulus. Note that by matching different SSP isochrones, we do not take into account the effect of the unresolved binaries or stellar rotation but focus on the possibility that

⁵ <http://ned.ipac.caltech.edu/>

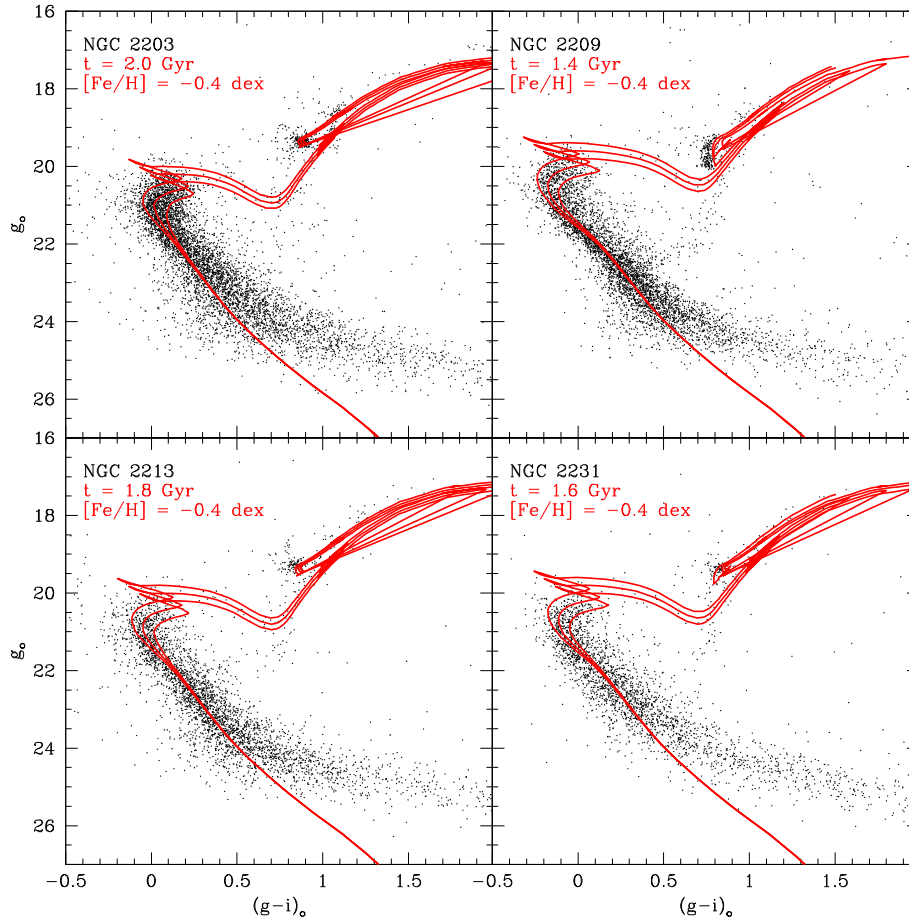


Figure 17. Theoretical isochrones from Bressan et al. (2012) superimposed on to LMC cluster CMDs. The youngest isochrone corresponds to $\log(t) - \sigma(\log(t))$ and metallicity (Z) listed in Table 16, whereas the isochrone separation is $\Delta(\log(t)) = 0.05$.

any unusual broadness at the MSTO might come from the presence of populations of different ages. Mackey et al. (2008), Milone et al. (2009), Goudfrooij et al. (2009), Piatti (2013), among others, showed that a significant fraction of unresolved binaries is not enough to reproduce the EMSTOs seen in their studied clusters, while stellar rotation has not driven the whole MSTO broadness in all the cases (Girardi et al. 2009; Li et al. 2014). Since the purpose of this work consists in introducing the high-quality deep photometric data set and provide with mean cluster ages from which we will study any possible extended MSTO cluster candidate, the matching of SSP isochrones results overall justified. Moreover, by closely inspecting the matched cluster MSTO regions, we have a hint for any uncommon broadness in the studied cluster sample.

In the matching procedure with a naked eye, we used seven different isochrones, ranging from slightly younger than the derived cluster age to slightly older. Finally, we adopted the cluster age as the age of the isochrone which best reproduced the cluster’s main features in the CMD (namely, the cluster’s MS, RCs, and/or RGBs). We noted, however, that the theoretically computed bluest stage during the He-burning core phase is redder than the observed RC in the CMDs of some clusters, a behaviour already detected in other studies of Galactic and Magellanic Cloud clusters (e.g. Piatti et al. 2009, Piatti et al. 2011a, Piatti et al. 2011b, and references therein). A similar outcome was found from the matching of isochrones in the M_V versus $(V - I)_0$ plane (Piatti, Clariá & Ahumada 2003a,b, among others). Figs 16–19 show the results of isochrone matching.

For each cluster CMD, we plotted the isochrone of the adopted cluster age and two additional isochrones bracketing the derived age and separated by $|\Delta(\log(t))| = 0.05$. The ages of the adopted isochrones for the cluster sample are listed in Table 16. For clusters with density ratio ($\rho =$ cluster star density to background field star density ratio at r_{HM}) greater than 1.0, the age uncertainty is estimated as 0.05 dex in $\log(t)$ while for clusters with larger background contamination, the uncertainty reaches 0.10 dex. These age uncertainties are thought to mainly represent the overall dispersion along the SGB, RGB as well as the position of the RC, rather than a measure of the MSTO spread. Nevertheless, in most of the clusters the adopted age uncertainties relatively reflect the observed MSTO broadness, thus implying a weaker chance for the EMSTO phenomenon. Note, however, that we have assigned the same mean age error to NGC 2173 and NGC 2209 – even though only the latter was confirmed as an EMSTO cluster by Keller et al. (2012) – simply because both clusters have ρ greater than 1.0. In the last two columns, we have compiled previously published age information. Fig. 20 shows the comparison between the published ages and our present values. The error bars correspond to the age uncertainties quoted by the authors, while the thick and thin lines represent the identity relationship and those shifted by ± 0.05 , respectively. Black filled squares represent clusters that do not fulfil the requirement $0.05 + \sigma(\log(t)_{\text{pub}}) \geq |\log(t)_{\text{our}} - \log(t)_{\text{pub}}|$. As can be seen, there is reasonable agreement ($|\text{present minus literature values}| = 0.12 \pm 0.10$), although three clusters significantly depart from the

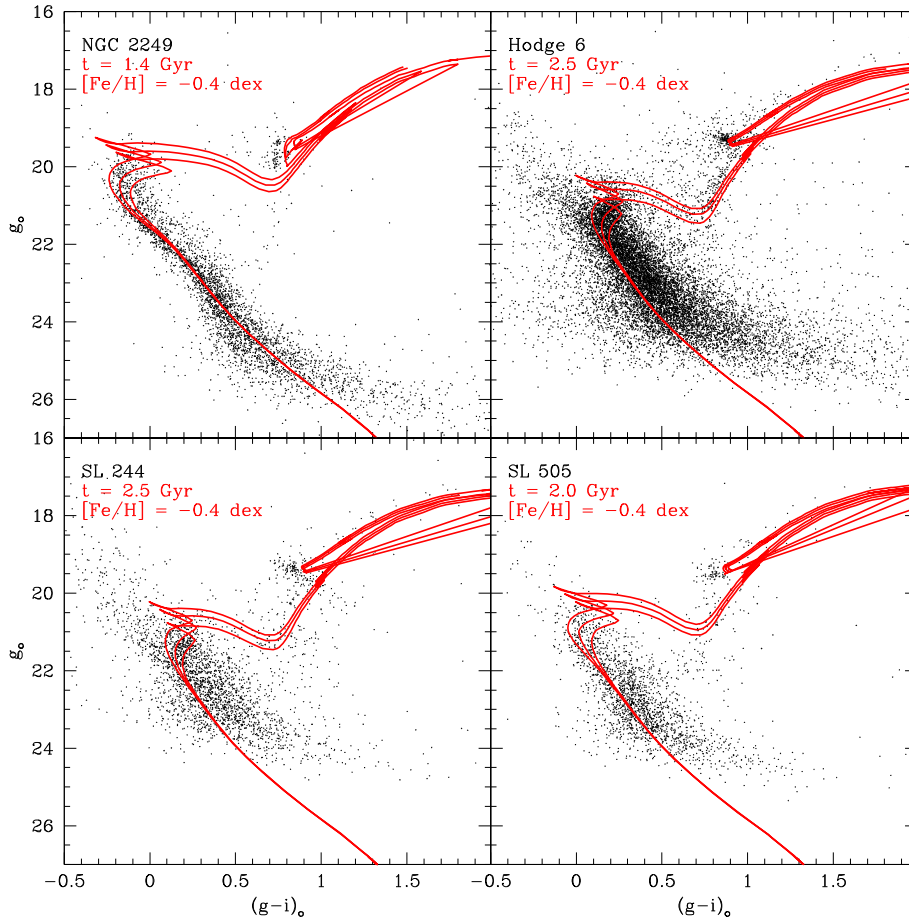


Figure 18. Theoretical isochrones from Bressan et al. (2012) superimposed on to LMC cluster CMDs. The youngest isochrone corresponds to $\log(t) - \sigma(\log(t))$ and metallicity (Z) listed in Table 16, whereas the isochrone separation is $\Delta(\log(t)) = 0.05$.

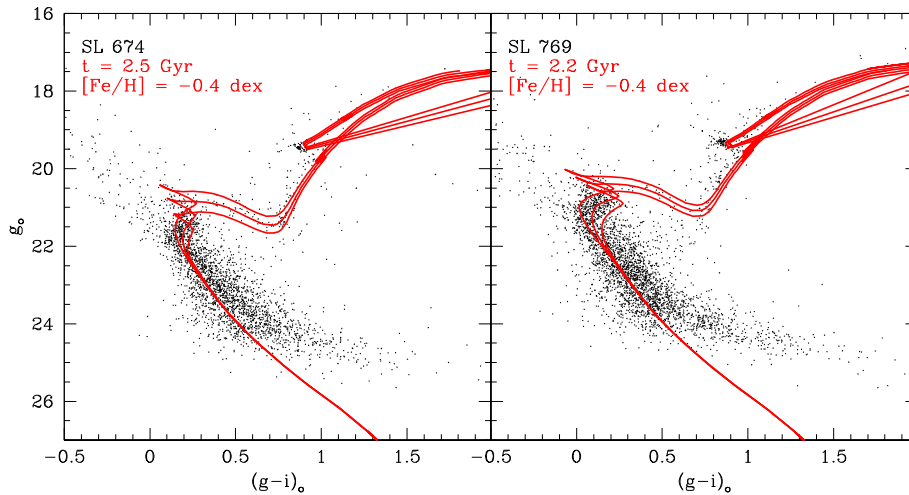


Figure 19. Theoretical isochrones from Bressan et al. (2012) superimposed on to LMC cluster CMDs. The youngest isochrone corresponds to $\log(t) - \sigma(\log(t))$ and metallicity (Z) listed in Table 16, whereas the isochrone separation is $\Delta(\log(t)) = 0.05$.

$\pm 1\sigma$ strip. In the case of NGC 2161 and SL 244, we checked that the younger ages by Geisler et al. (2003) and Piatti et al. (2011a), respectively, are related to a much less deep photometry which barely reach the cluster MSTOs. In this sense, our age estimates surpass in accuracy those previously derived. On the other hand, our age determination for NGC 2249 is significantly older than that

determined by Baumgardt et al. (2013) but in line with the stated uncertainties of that work. Finally, by looking at fig. 2 of Keller et al. (2012), the mean age of NGC 2209 is $\log(t) \approx 9.06$ dex, whereas we estimate a slightly older value (9.15). For NGC 2173 the agreement is better: $\log(t) \approx 9.22$ from their fig. 2 and 9.25 from our Table 16.

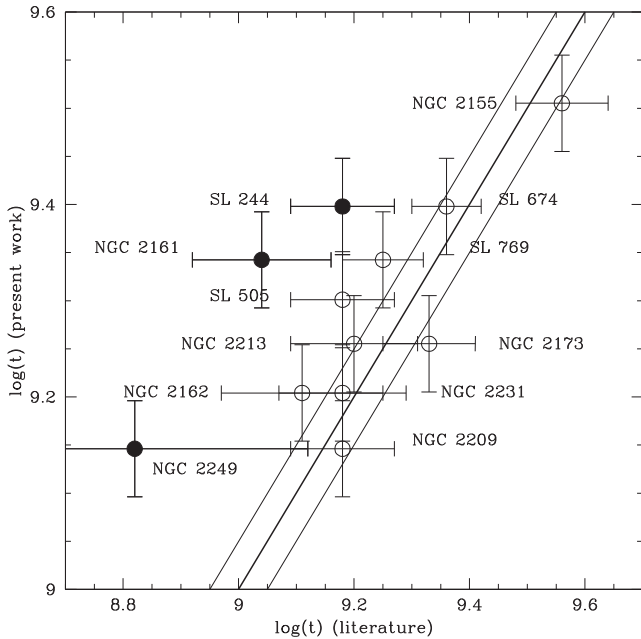


Figure 20. Comparison of LMC cluster ages determined in this work with those available in the literature. The straight line represents the 1:1 relationship.

5 SUMMARY

As part of a continuing project to investigate the extended MSTO phenomenon that is seen to be widespread in intermediate-age LMC clusters, we have used the Gemini South telescope to obtain GMOS imaging in the SDSS g , i system of 14 candidate intermediate-age LMC star clusters. Our aim is to establish a luminosity-limited sample of clusters in the age range of 1–3 Gyr in which to characterize the prevalence of the extended MSTO phenomenon. In this work, we present the CMDs of NGC 2155, 2161, 2162, 2173, 2203, 2209, 2213, 2231, 2249, Hodge 6, SL 244, 505, 674, and 769. The analysis of their photometric data leads to the following main conclusions.

(i) After extensive artificial star tests over the image data set, we show that the 50 per cent completeness level is reached at g , $i \sim 23.5$ – 25.0 , depending on the distance to the cluster centre, and that the behaviour of the photometric errors with magnitude for the observed stars guarantees the accuracy of the morphology and position of the main features in the CMDs that we investigate.

(ii) We trace their stellar density radial profiles from star counts performed over the GMOS field of view. From the density profiles, we adopted cluster radii defined as the distance from the cluster centre where the stellar density profile intersects the background level, and derived the radii at the FWHM of the radial profile. We then built CMDs with cluster features clearly identified.

(iii) Using the cluster (g , $g - i$) diagrams, we estimated ages from theoretical isochrones computed for the SDSS system. The studied LMC clusters are confirmed to be intermediate-age clusters of age, $\log(t) = 9.10$ – 9.60 ; we identified two of them, namely NGC 2162 and 2249, to be new extended MSTO cluster candidates on the basis of their dual RCs.

ACKNOWLEDGEMENTS

This work was partially supported by the Argentinian institutions CONICET and Agencia Nacional de Promoción Científica y

Tecnológica (ANPCyT). SCK and GDC acknowledge the support of Australian Research Council (ARC) Discovery Project grant DP120101237. ADM is grateful for support from an ARC Australian Research Fellowship (DP1093431). Based on observations obtained at the Gemini Observatory (programmes: GS-2011A-Q-43, GS-2012A-Q-15, and GS-2013A-Q-17), which is operated by the Association of Universities for Research in Astronomy, Inc., under a cooperative agreement with the NSF on behalf of the Gemini partnership: the National Science Foundation (United States), the Science and Technology Facilities Council (United Kingdom), the National Research Council (Canada), CONICYT (Chile), the Australian Research Council (Australia), Ministério da Ciência, Tecnologia e Inovação (Brazil) and Ministerio de Ciencia, Tecnología e Innovación Productiva (Argentina). We thank the anonymous referee whose comments and suggestions allowed us to improve the manuscript.

REFERENCES

- Bastian N., de Mink S. E., 2009, *MNRAS*, 398, L11
 Bastian N., Silva-Villa E., 2013, *MNRAS*, 431, L122
 Baumgardt H., Parmentier G., Anders P., Grebel E. K., 2013, *MNRAS*, 430, 676
 Bica E., Geisler D., Dottori H., Piatti A. E., Clariá J. J., Santos J. F. C., Jr, 1998, *AJ*, 116, 723
 Bressan A., Marigo P., Girardi L., Salasnich B., Dal Cero C., Rubele S., Nanni A., 2012, *MNRAS*, 427, 127
 Burstein D., Heiles C., 1982, *AJ*, 87, 1165 (BH)
 Cabrera-Ziri I., Bastian N., Davies B., Magris G., Bruzual G., Schweizer F., 2014, *MNRAS*, 441, 2754
 Cardelli J. A., Clayton G. C., Mathis J. S., 1989, *ApJ*, 345, 245
 Carretta E., Bragaglia A., Gratton R. G., Recio-Blanco A., Lucatello S., D’Orazi V., Cassisi S., 2010, *A&A*, 516, 55
 Da Costa G. S., 1991, in Haynes R., Milne D., eds, *Proc. IAU Symp.* 148, The Magellanic Clouds. Kluwer, Dordrecht, p. 183
 de Grijs R., Wicker J. E., Bono G., 2014, *AJ*, 147, 122
 Geisler D., Piatti A. E., Bica E., Clariá J. J., 2003, *MNRAS*, 341, 771
 Girardi L., Rubele S., Kerber L., 2009, *MNRAS*, 394, L74
 Goudfrooij P., Puzia T. H., Kozhurina-Platais V., Chandar R., 2009, *AJ*, 137, 4988
 Keller S. C., Mackey A. D., Da Costa G. S., 2011, *ApJ*, 731, 22
 Keller S. C., Mackey A. D., Da Costa G. S., 2012, *ApJ*, 761, L5
 Li Ch., de Grijs R., Deng L., 2014, *ApJ*, 784, 157
 Mackey A. D., Broby Nielsen P., 2007, *MNRAS*, 379, 151
 Mackey A. D., Broby Nielsen P., Ferguson M. N., Richardson J. C., 2008, *ApJ*, 681, L17
 Milone A. P., Bedin L. R., Piotto G., Anderson J., 2009, *A&A*, 497, 755
 Piatti A. E., 2013, *MNRAS*, 430, 2358
 Piatti A. E., Geisler D., 2013, *AJ*, 144, 100
 Piatti A. E., Geisler D., Bica E., Clariá J. J., Santos J. F. C., Jr, Sarajedini A., Dottori H., 1999, *AJ*, 118, 2865
 Piatti A. E., Sarajedini A., Geisler D., Bica E., Clariá J. J., 2002, *MNRAS*, 329, 556
 Piatti A. E., Clariá J. J., Ahumada A. V., 2003a, *MNRAS*, 340, 1249
 Piatti A. E., Clariá J. J., Ahumada A. V., 2003b, *MNRAS*, 346, 390
 Piatti A. E., Clariá J. J., Parisi M. C., Ahumada A. V., 2009, *New Astron.*, 14, 97
 Piatti A. E., Clariá J. J., Parisi M. C., Ahumada A. V., 2011a, *PASP*, 123, 519
 Piatti A. E., Clariá J. J., Bica E., Geisler D., Ahumada A. V., Girardi L., 2011b, *MNRAS*, 417, 1559
 Schlafly E. F., Finkbeiner D. P., 2011, *ApJ*, 737, 103
 Schlegel D. J., Finkbeiner D. P., Davis M., 1998, *ApJ*, 500, 525
 Stetson P. B., Davis L. E., Crabtree D. R., 1990, in Jacoby G. H., ed., *ASP Conf. Ser. Vol. 8, CCDs in Astronomy*. Astron. Soc. Pac., San Francisco, p. 289

Subramanian S., Subramanian A., 2009, *A&A*, 496, 399
Yang W., Meng X., Bi Sh., Tian Z., Li T., Liu K., 2011, *ApJ*, 731, L37

SUPPORTING INFORMATION

Additional Supporting Information may be found in the online version of this article:

Tables 2–15. CCD *gi* data of stars in the field of NGC 2155. The complete table is available online as Supporting Infor-

mation (<http://mnras.oxfordjournals.org/lookup/suppl/doi:10.1093/mnras/stu1535/-/DC1>).

Please note: Oxford University Press are not responsible for the content or functionality of any supporting materials supplied by the authors. Any queries (other than missing material) should be directed to the corresponding author for the article.

This paper has been typeset from a $\text{\TeX}/\text{\LaTeX}$ file prepared by the author.